Article

Cover Crop Biomass Predictions with Unmanned Aerial Vehicle Remote Sensing and TensorFlow Machine Learning

Aakriti Poudel [1], Dennis Burns [2], Rejina Adhikari [1], Dulis Duron [1], James Hendrix [2], Thanos Gentimis [3], Brenda Tubana [1] and Tri Setiyono [1,*]

1 School of Plant, Environmental and Soil Sciences, Louisiana State University, Baton Rouge, LA 70803, USA; apoudel@agcenter.lsu.edu (A.P.)
2 Northeast Research Station, Louisiana State University Agricultural Center, St. Joseph, LA 71366, USA
3 Department of Experimental Statistics, Louisiana State University, Baton Rouge, LA 70803, USA
* Correspondence: tsetiyono@agcenter.lsu.edu; Tel.: +1-225-578-3135

Abstract: The continuous assessment of cover crop growth throughout the season is a crucial baseline observation for making informed crop management decisions and sustainable farming operation. Precision agriculture techniques involving applications of sensors and unmanned aerial vehicles provide precise and prompt spectral and structural data, which allows for effective evaluation of cover crop biomass. Vegetation indices are widely used to quantify crop growth and biomass metrics. The objective of this study was to evaluate the accuracy of biomass estimation using a machine learning approach leveraging spectral and canopy height data acquired from unmanned aerial vehicles (UAVs), comparing different neural network architectures, optimizers, and activation functions. Field trials were carried out at two sites in Louisiana involving winter cover crops. The canopy height was estimated by subtracting the digital surface model taken at the time of peak growth of the cover crop from the data captured during a bare ground condition. When evaluated against the validation dataset, the neural network model facilitated with a Keras TensorFlow library with Adam optimizers and a sigmoid activation function performed the best, predicting cover crop biomass with an average of 96 g m^{-2} root mean squared error (RMSE). Other statistical metrics including the Pearson correlation and R^2 also showed satisfactory conditions with this combination of hyperparameters. The observed cover crop biomass ranged from 290 to 1217 g m^{-2}. The present study findings highlight the merit of comprehensive analysis of cover crop traits using UAV remote sensing and machine learning involving realistic underpinning biophysical mechanisms, as our approach captured both horizontal (vegetation indices) and vertical (canopy height) aspects of plant growth.

Keywords: cover crops; biomass; vegetation indices; canopy height; TensorFlow; deep learning

1. Introduction

Cover crops are the crops that are planted when soil is fallow between main crops [1]. They are grown with the purpose of enhancing soil and crop production as well as providing many other agroecosystem services rather than a cash crop. This reduces nitrogen leaching [2] and enhances organic matter, carbon dynamics, and microbial processes in soil [3]. Among cover crops, legumes consistently add nitrogen to soil, whereas grasses and brassica scavenge residual nitrogen, as is evident by reduced nitrate and increased ammonium in spring soil, which will eventually become available to subsequent crops [4]. The goal of cover cropping varies according to the needs of growers. Farmers can grow

legumes for enhanced nutrient availability to subsequent cash crops, cereal cover crops for large biomass production to aid soil organic matter buildup, or brassica species to control soil-borne pests [5].

One of the most well-established roles of cover crops in crop production is the weed suppression and agrochemical reduction potential [6]. Other ecosystem services include an enhancement of pollination resources [7,8]. Furthermore, a cover crop may be used as forage and feed for animal production to generate revenue without land use change [9]. However, these crops are not primarily intended for yield generation; biomass production is tied with ecological and agronomic functions, and the benefits they can offer vary based on the amount of biomass production and the types of crop species [10].

The prediction of cover crop biomass is needed for the quantification of its benefit as an agricultural input and to better understand how much it aids soil properties and subsequent crop productivity. Cover crops can only reduce nutrient loss if adequate biomass can be established [11]. Biomass production is positively correlated with nitrogen retention [12]. Researchers and growers target higher biomass production for enhancing the inherent agroecosystem services [13]. To suppress the most weeds and achieve optimal nitrogen retention, biomass should ideally reach 4.6 Mg ha^{-1} and 6.9 Mg ha^{-1} respectively [13].

It is crucial to assess biomass, as it can be a proxy for estimating canopy cover, which means a higher soil coverage, reduced nutrient leaching and erosion, and improved weed suppression. This prediction is useful to identify areas with high weed pressure in the field, which need intervention to enhance precision weed management strategies. There is growing interest in estimating crop biomass utilizing remotely sensed imagery for prompt and precise quantification. By leveraging UAV images and machine learning, the models for biomass prediction and weed assessment can be refined. The benefits can be significantly enhanced via timely monitoring of the cover crops biomass through remote sensing [14]. Destructive field sampling and laboratory analysis are costly and labor intensive, especially when spatial variability is considered within the field.

Among recent technological advancements, the UAV has allowed an unparalleled level of crop analysis by serving as a reliable measure for harvested biomass in later stages of crop growth [15]. Remote sensing of vegetation is an established approach for understanding the plant status in terms of health, growth, stress, water use efficiency, and production [16]. It is a widely established approach for estimating crop biomass, which involves calculating vegetation indices (VIs) involving near-infrared (NIR) reflectance [17,18]. Vegetation indices including the NDVI (Normalized Vegetation Index), G-R (Green–Red Vegetation Index), GNDVI (Green Normalized Differential Vegetation Index), and SAVI (Soil-Adjusted Vegetation) are efficient for low to medium biomass range prediction whereas the TVI (Triangular Vegetation Index) can be used for later stages with high biomass points [19].

Biomass estimation is more accurate, with narrow band vegetation indices, which do not have a saturation problem [20,21]. Studies have successfully estimated the aboveground vegetation of winter cover crops [19,22] through suitable remotely sensed indices. Remote-sensed vegetation indices are simple yet effective evaluation algorithms for the canopy cover, robustness, and other growth dynamics. They are good indices for plant height estimation; however, they lack sensitivity in the later stages of plant growth [23]. The common imagery datasets obtained from fields allow for estimates of many other traits of cover crops. Canopy height (CH), one of the most important phenotypic traits of crops, can be effectively captured by UAVs by assessing spatial auxiliary information including digital terrain and surface models [24]. This approach is flexible as the canopy height can still be estimated when a DTM is not available [25,26] and a ground control point cannot be set for geo-referencing [27]. For this study, the cover crop modeled canopy height (CHM) was estimated using a digital surface model (DSM) derived from unmanned aerial

vehicle (UAV) red green blue (RGB) images. Crop biomass data are known to be associated with the UAV-derived CHM [28]. Others have attempted to combine VIs and the CHM to estimate crop biomass [28,29]. The artificial neural network (ANN) is an ideal model to capture complex non-linear relationships between multiple predictors and the target attribute(s) [30]. The resulting predictions should be accurate and driven by reasonable underpinning mechanisms identified via feature selection [31].

The objective of this study was to craft a machine learning model using spectral and structural inputs from UAVs to enhance prediction accuracy. We compared prediction errors, as measured by RMSE, and identified the most effective model configuration through the evaluation of different optimizers and activation functions. This study addressed a research gap by integrating an advanced technology and methodology for data-driven and reliable cover crop assessment.

2. Materials and Methods

2.1. Data Collection

This study was conducted during winter (October 2023 to March 2024) at LSU AgCenter Northeast Research Station, St. Joseph, LA, USA (NERS, 31°56′47.998″ N, 91°13′49.688″ W, 2 m above sea level) and LSU AgCenter Doyle Chambers Central Research Station, Baton Rouge, LA, USA (CRS, 30°21′51.826″ N, 91°9′52.999″ W, 5 m above sea level) (Figure 1). At NERS, cover crops were a mix of cereal rye (*Secale cereale* L.), daikon radish (*Raphanus sativus*), hairy vetch (*Vicia villosa*), winter peas (*Pisum sativum*), faba beans (*Vicia faba*), white mustard (*Sinapis alba*), Triticale (*Triticum secale*), and Safflower (*Carthamus tinctorius*). At CRS, the summer cropping system was a corn (*Zea mays*) and soybean (*Glycine max* L.) rotation, whereas at NERS, the summer cropping system was a corn (*Zea mays*), soybean (*Glycine max* L.), and cotton (*Gossypium hirsutum*) rotation. Cover crops were a monoculture of black oats (*Avena strigosa*) and cereal rye (*Secale cereale* L.) in fields 31 and 33 at CRS, respectively (Figure 1b). At the time of biomass prediction, in late March at NERS, only the following cover crop species had substantial biomass: cereal rye, daikon radish, white mustard, and Triticale, while the other species were either non-existent or had negligible biomass due to natural termination.

Cover crop biomass was collected by cutting the plants at the ground surface using a 0.5 × 0.5 m quadrant. The sampling quadrant was equipped with a central marking spot for collection of cm-level-precision geographic coordinate data using an EMLID RS2 Global Navigation Satellite System (GNSS) Real-Time Kinematic (RTK) instrument (EMLID Tech Kft., Budapest, Hungary) following biomass data collection. The sampling spots were scattered across the study field (Figure 1). The gaps where no biomass data were collected at NERS (Figure 1a) were associated with a separate study with different ground surface conditions. At CRS, the gaps where no samples were collected (Figure 1b) were associated with the sections of the fields kept fallow during the winter season (part of another study comparing the long-term impact of a cover crop vs. fallow in the corn–soybean cropping system). A total of 174 and 144 data points were taken at CRS on March 26 and 27, 2024 and at NERS on March 27 and 28, 2024, respectively. The plant samples were kept in the dryer at 68 °C for 48 h prior to recording the dry matter weight with an HC30002X Digital Scale (Fristaden Lab, Reno, NV, USA).
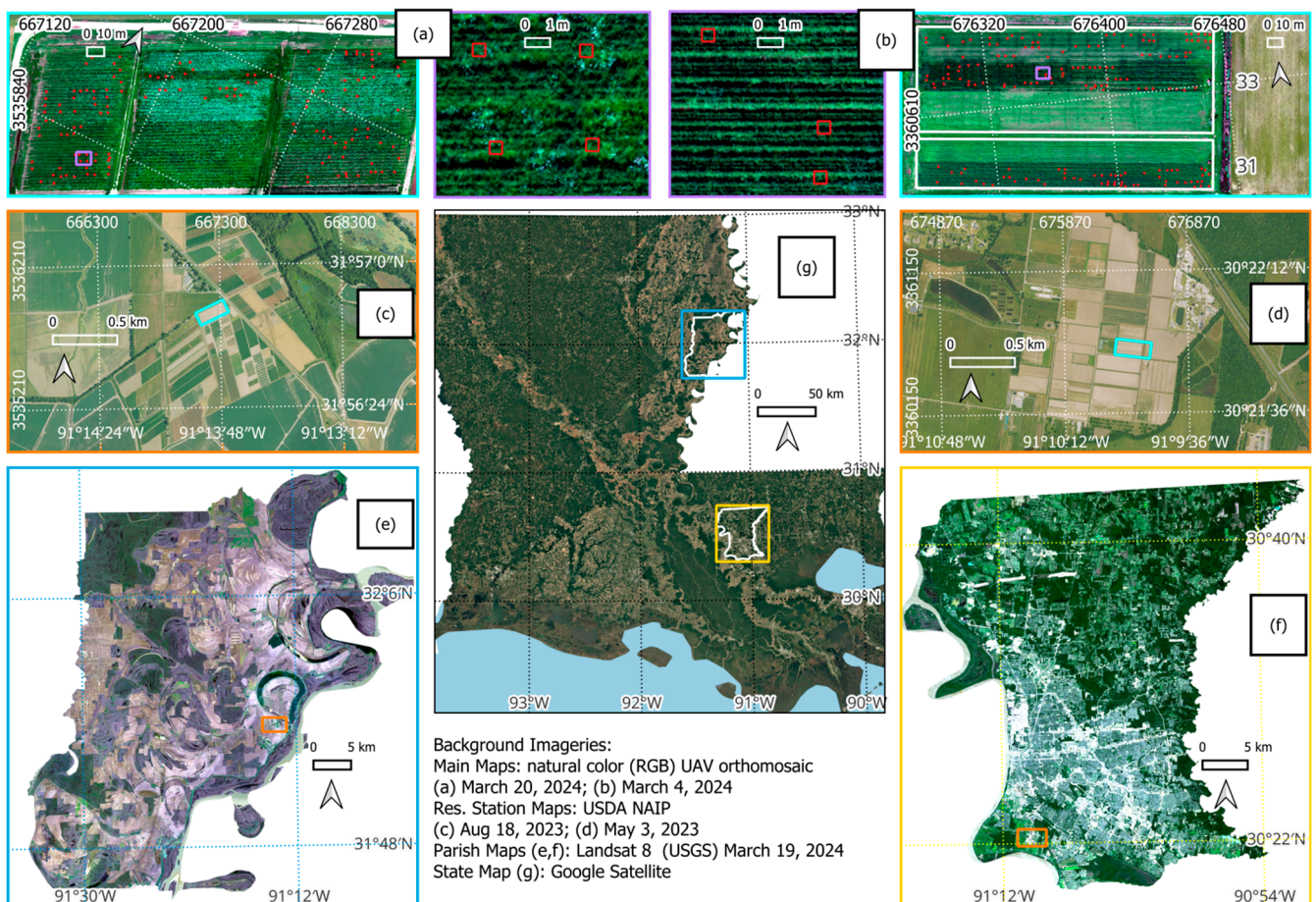
Figure 1. Cover crop biomass prediction study sites with inset maps showing examples of sampling distributions. (**a**) Northeast Research Station (NERS) in Tensas parish, LA. (**b**) Central Research Station in East Baton Rouge parish, LA. The coordinate reference system (CRS) used was EPSG 32615 (Universal Transfer Mercator, UTM, zone 15 with World Geodetic System, WGS, 1984 ensemble datum). Reference easting and northings are shown in the maps of the fields (**a**,**b**) and the station maps (**c**,**d**). The corresponding reference geographic coordinates are shown in all maps except for the inset maps. Red squares in (**a**,**b**) indicate the biomass sampled locations with detailed shown in the inset maps (highlighted as purple rectangles). Cyan rectangles in (**c**,**d**) highlight the location of the study fields in the station overview maps. Orange rectangles in (**e**,**f**) highlight the location of NRS and CRS in the corresponding parishes. Yellow rectangles in (**g**) highlight the location of the East Baton Rouge and Tensas parishes in Louisiana.

In this study, vegetation indices (VIs) were derived from multispectral data (Table 1) [32–35], and the modeled canopy plant height (CHM) was derived from digital surface model (DSM) products of the RGB data-processing chain in Pix4D Mapper version 4.7.5 [36]. The acquisition of multispectral (Blue at 475 nm, Green at 560 nm, Red at 668 nm, Red Edge at 717 nm, and NIR at 840 nm) and RGB data was facilitated with MicaSense Red-Edge MX (Seattle, WA, USA), DJI H20 (Shenzhen, China), and DJI Matrice 300 RTK multirotor Unmanned Aerial Vehicle (UAV) aircraft. The UAV mapping missions were programmed at 40 m altitude using DJI Pilot 2 version 5.1.1.7. Four ground control points (GCPs) were placed at the corners of the study area, and geographic coordinate data were measured using an EMLID Reach RS2 GNSS RTK instrument with base correction using NASA OPUS version 5.0.0 (https://www.ngs.noaa.gov/OPUS/) (accessed on 28 June 2023) and a geographic optimization process in Pix4D Mapper [37]. Following the generation of orthomosaic reflectance data, the Geospatial Data Abstraction Library (GDAL) [38] was used to generate composite layers from the five spectral bands. Multispectral imagery was used for computation of the vegetation indices using raster calculator in QGIS version 3.28.1 [39].

CHM was generated by subtracting the DSM output taken in the bare ground condition from the output taken at the time of peak cover crop growth. Universal Transfer Mercator (UTM) zone 15 based on the World Geodetic System (WG) 1984 ensemble datum (EPGS 32615) was used as the projection and coordinate reference system for the spatial data in this study. The data-sanitizing process in this study included the removal of outlier pixels with an NDRE value less than 0.2, given that such NDRE values indicate non-plant surfaces, namely, exposed ground [40].

Table 1. Vegetation indices used in this study. In-progress.

Name	Vegetation Index Description	Equation	Ref.
NDRE	Normalized Difference Red Edge	$(NIR - RE)/(NIR + RE)$	[32]
GNDVI	Green Normalized Difference Vegetation Index	$(NIR - G)/(NIR + G)$	[33]
NDVI	Normalized Difference Vegetation Index	$(NIR - R)/(NIR + R)$	[34]
PVI	Perpendicular Vegetation Index	$\sqrt{(NIR - R)^2 + (R - NIR)^2}$	[35]
VIG	Vegetation Index Green	$G/(R + B)$	[33]

NIR, Near-Infrared (840 nm); RE, Red Edge (717 nm); G, Green (560 nm); R, Red (668 nm); B, Blue (475 nm).

2.2. Model Description

The overall cover crop prediction model used in this study is shown in Figure 2. Five vegetation indices (NDRE, GNDVI, NDVI, PVI, and VIG) and the modeled canopy height (CHM) are used as inputs for the machine learning model, with training, validation, and testing split set at 50–25–25. This training split follows the suggested setting for such a data usage configuration in machine learning [41].
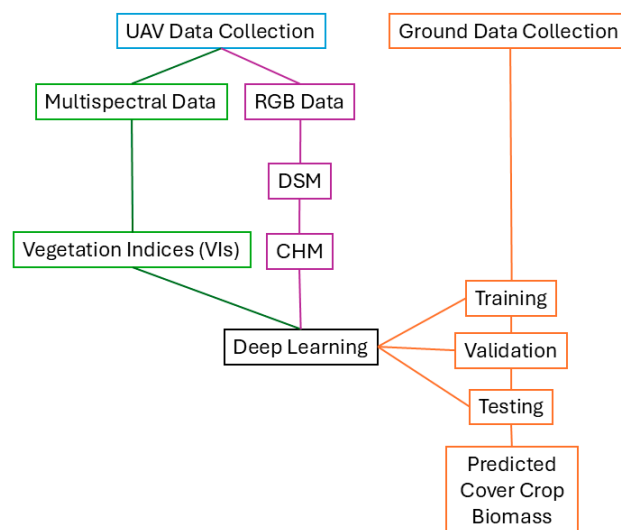

Figure 2. The workflow of the cover crop biomass prediction model in this study. UAV, unmanned aerial vehicle. RGB, red green blue or natural color aerial imagery data. DSM, digital surface model. CHM, modeled canopy height.

In this study, the different hyperparameter configurations of a deep neural network were explored, facilitated by the Keras and TensorFlow libraries [42]. The performance levels of these models in predicting cover crop biomass as a function of VIs and the CHM were compared. The metric for accuracy performance was based on the root mean square error between the predicted (test results) and measured cover crop biomass. The basic structure of the Tensor network had 11 dense layers, with the number of batches and fixed activation functions shown in Figure 3. The fixed and dynamic hyperparameters (8 optimizers and 8 activation functions) are detailed in Table 2 [43–51]. The architectural configuration was informed by similar previous studies and an initial analysis of similar datasets, and it strikes a balance between accuracy and timeliness. For each configuration

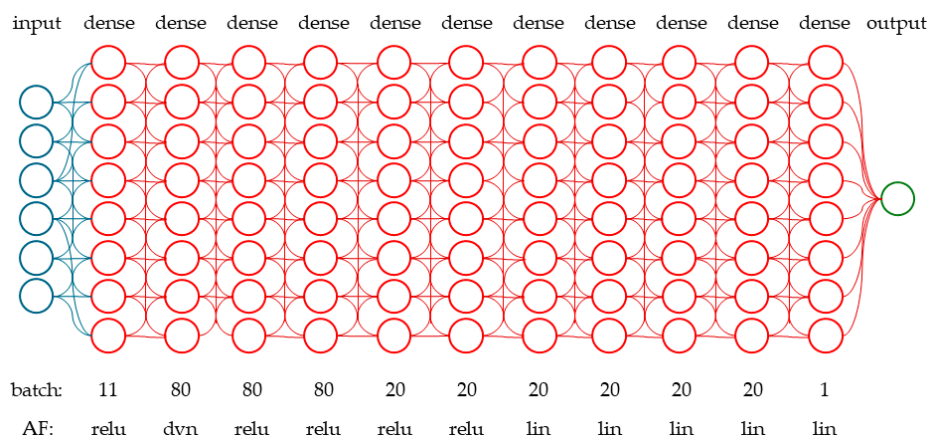of the dynamic hyperparameters, the model was run 3 times, with the best results chosen as the final output.

Figure 3. The neural network diagram of the TensorFlow machine learning for cover crop biomass prediction in this study. The top line indicates the different layers including the input, 11 dense layers, and the output layer. The batch number associated with each dense layer is shown at the bottom line together with activation function (AF) information including the rectified linear unit (relu), dynamic functions (see Table 2, dyn), and linear function (lin).

Table 2. The hyperparameters of the Keras TensorFlow machine learning for cover crop biomass prediction in this study.

Aspect	Parameter	Details [2]
Fixed:		
Split	0.5, 0.25, 0.25	50% training, 25% validation, 25% testing
Epoch	200	Number of complete passes of the training dataset
Learning rate	0.001	Hyperparameter controlling how much to change the model in response to the estimated error each time the model weights are updated
Dynamic:		
Optimizers	Adam	Adaptive Moment Estimation. Stochastic gradient descent method based on adaptive estimation of first-order and second-order moments [43]
	Nadam	Nesterov-accelerated Adaptive Moment Estimation [44]
	Ftrl	Follow the (Proximally) Regularized Leader. Online gradient descent with alternative regularization of model parameters [45]
	SGD	Stochastic Gradient Descent. Iterative optimization process to search optimum outputs [46]
	RMSprop	Root Mean Square Propagation. Adaptive learning optimization to improve performance and learning speed [47]
	Adadelta	Stochastic gradient descent method based on the adaptive learning rate per dimension, which works by improving learning rates throughout training and making use of global learning rate [48]
	Adagrad	Optimizer with parameter-specific learning rates that are adapted relative to how frequently a parameter is updated during training [49]
	Adamax	Alternation of Adam optimizer with adaptive approximation of low-order moments based on the infinity norm [43]
AF [1]	Sigmoid	$f(x) = 1/(1 + e^{-x})$; [46]
	Tanh	$f(x) = \sin x / \cos x$; [46]
	ReLU	$f(x) = max(0, x)$; Rectified Linear Unit [46]
	Exponential	$f(x) = e^x$; [46]
	Linear	$f(x) = x$; [46]
	SELU	$f(x) = \begin{cases} sx, & x > 0 \\ s\alpha(e^x - 1), & x \le 0 \end{cases}$; Scaled Exponential Linear Unit [50]
	ELU	$f(x) = \begin{cases} x, & x > 0 \\ e^x - 1, & x \le 0 \end{cases}$; Exponential Linear Unit [46]
	SiLU	$\begin{cases} f(x) = x\,\sigma(x) \\ \sigma(x) \text{ is logistic sigmoid} \end{cases}$; Sigmoid Linear Unit [51]

[1] AF, Activation Function; [2] *x*, Input Tensor; *s* = 1.05070098; *α* = 1.67326324.

3. Results

The spatial variability and the histograms of remote-sensing data used in this study are shown in Figures 4 and 5 for the NRRS and CRS sites, respectively. As shown in the histogram data, the NDRE at NERS had a single peak (Figure 4a), while there were two peaks at CRS (Figure 5a). At both sites, the GNDVI and especially the NDVI data exhibited skewness toward high values (Figure 4b,c and Figure 5b,c). At NERS, the PVI histogram indicates a slightly off-center peak toward the high values (Figure 4d), unlike the PVI at the CRS site, with a peak closer to the center (Figure 5d). The variable VIG, on the other hand, showed the opposite trend, with the histogram for NERS slightly off-center toward the low values (Figure 4e), unlike the VIG at the CRES site, with a peak closer to the center (Figure 5e). The plant height estimate (PLH) at NERS showed dual peaks, with the dominant one skewed toward the high values (Figure 4f), whereas at CRS, the peak was toward the low values (Figure 5f). All vegetation indices except for VIG showed general similarity in their spatial patterns. The orthomosaic maps reveal four distinct spatial patterns exhibited by the remotely sensed data used in this study. The first pattern is shared among the NDRE, GNDI, and NDVI. The second, third, and fourth patterns are shown by the PVI, VIG, and CHM, respectively (Figures 4 and 5).
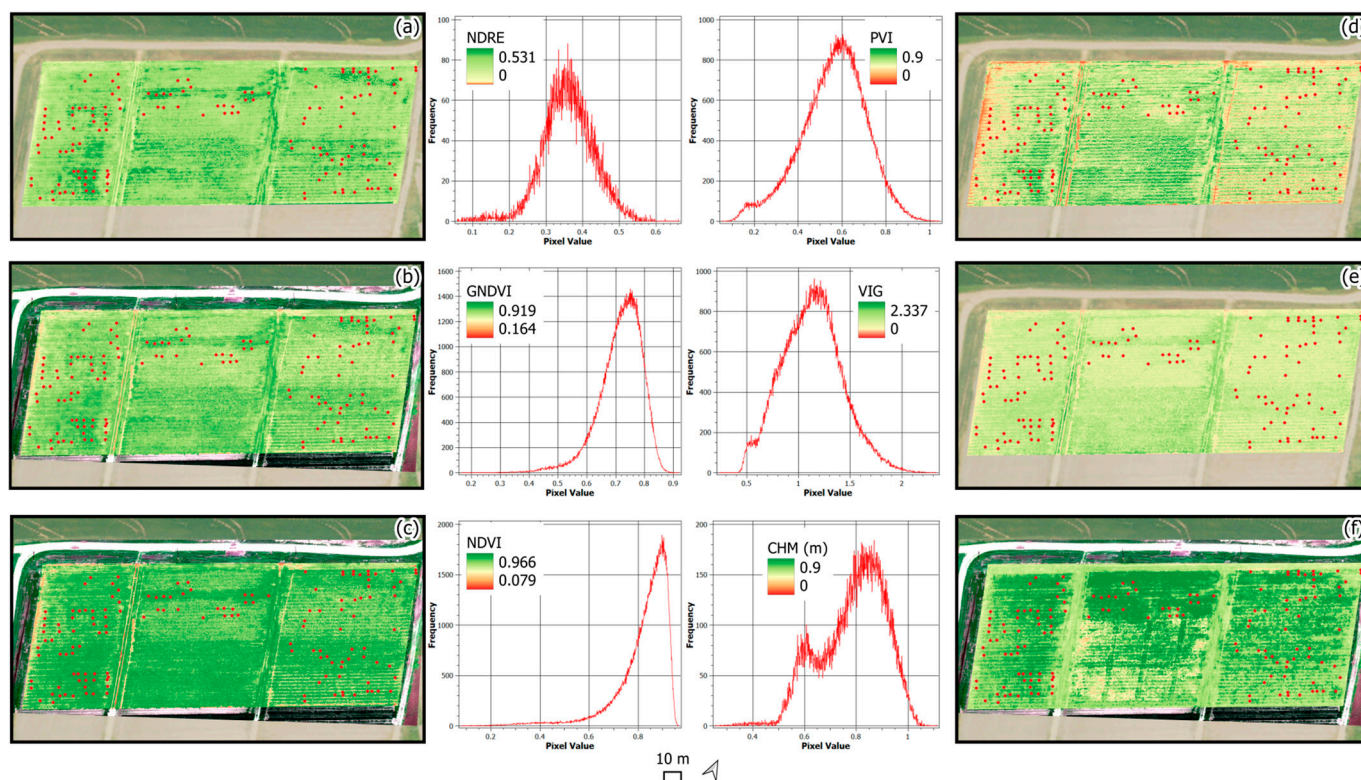

Figure 4. Spatial variability and histogram of remote-sensing data used in this study at NERS (20 March 2024). (**a**) NDRE, Normalized Difference Red Edge. (**b**) GNDVI, Green Normalized Difference Vegetation Index. (**c**) NDVI, Normalized Difference Vegetation Index. (**d**) PVI, Perpendicular Vegetation Index. (**e**) VIG, Vegetation Index Green. (**f**) CHM, Modeled Canopy Height.
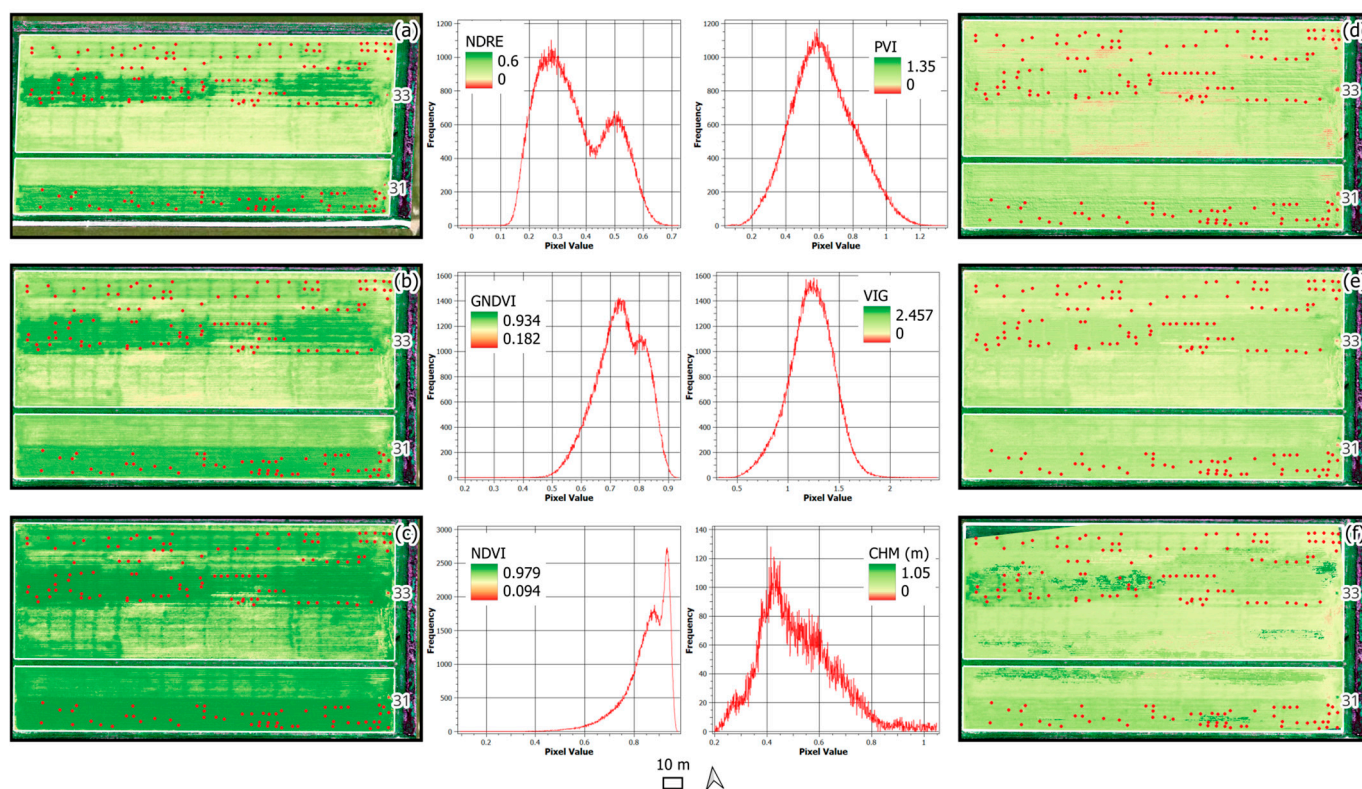
Figure 5. Spatial variability and histogram of remote-sensing data used in this study at CRS (6 March 2024). (**a**) NDRE, Normalized Difference Red Edge. (**b**) GNDVI, Green Normalized Difference Vegetation Index. (**c**) NDVI, Normalized Difference Vegetation Index. (**d**) PVI, Perpendicular Vegetation Index. (**e**) VIG, Vegetation Index Green. (**f**) CHM, Modeled Canopy Height.

The progress of the neural network model configuration, when trained utilizing the sampled remotely sensed data and cover crop dry matter (DM), based on the different optimizers and activation functions is shown in Figures 6 and 7, respectively. In these figures, the training results (root mean squared errors (RMSEs) of the predictions) are shown for the entire 200 epochs, with the first 40 epochs shown in detail in the inset graphs. From the initial RMSE of 578 g m^{-2}, when using default parameters, the model performance reached RMSE 131 g m^{-2}, with Adam performing the best among the optimizers tested at RMSE 124 g m^{-2} and Adadelta performing the worst at RMSE 138 g m^{-2} (Figure 6). All optimizers showed an early drop in RMSE at epoch 2, except for Adadelta. The optimizers Nadam, Ftrl, SGD, RMSprop, and Adadelta showed relatively slower RMSE improvement in the first 15 epochs as compared to Adam, Adagrad, and Adamax. The average ultimate RMSE at epoch 200 among the different activation functions was 131 g m^{-2}, with sigmoidal performing the best at RMSE 124 g m^{-2} and the linear activation function performing the worst at RMSE 140 g m^{-2} (Figure 7). The pattern of training progress, at least in the first 40 epochs, was strongly determined by the choice of optimizers rather than the activation functions, as shown in Figures 6 and 7.
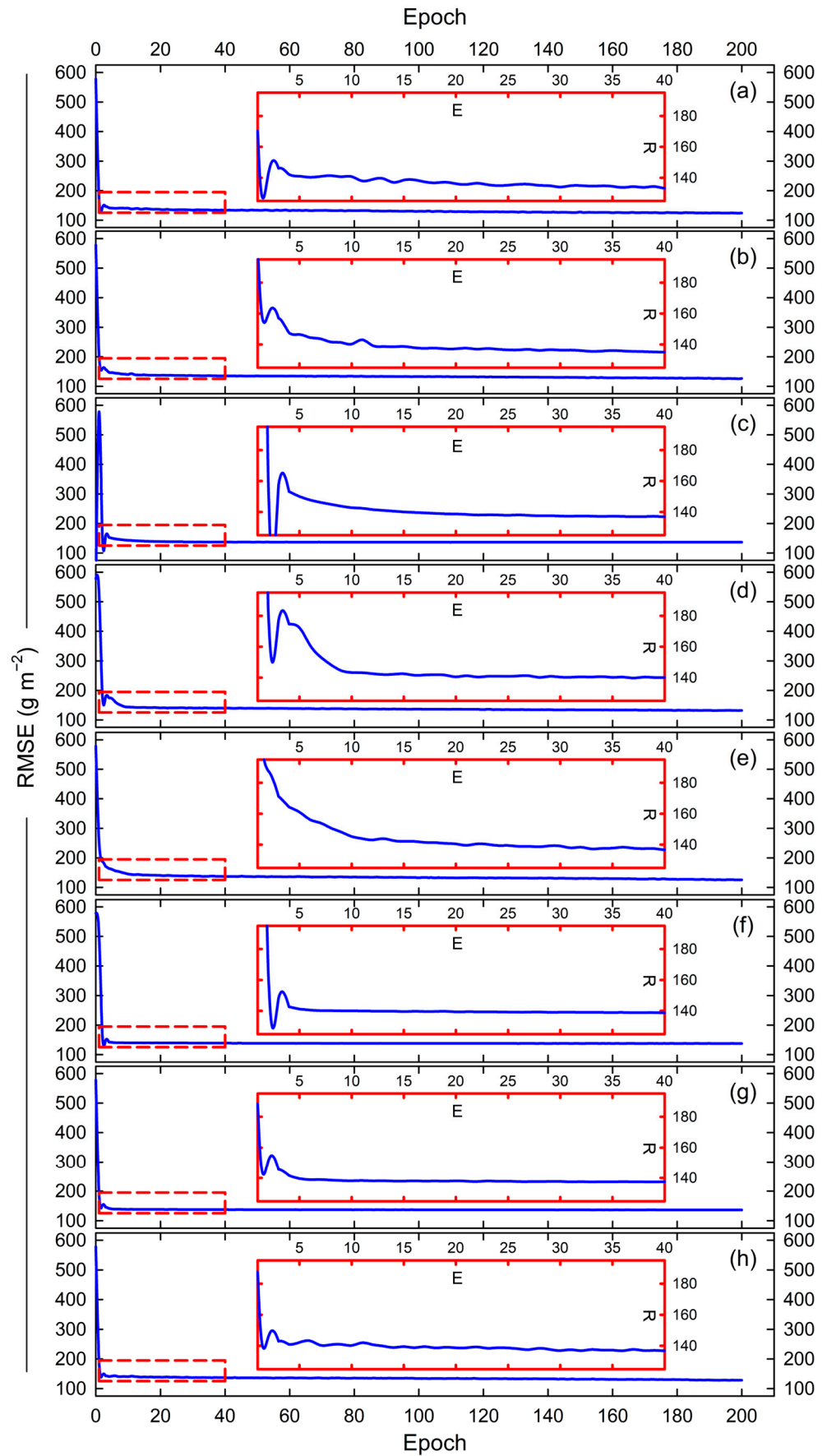
Figure 6. TensorFlow training progresses to predict cover crop biomass with Adam (**a**), Nadam (**b**), Ftrl (**c**), SGD (**d**), RMSprop (**e**), Adadelta (**f**), Adagrad (**g**), and Adamax (**h**) Keras optimizers. Detailed results within the first 40 epochs (E) are shown in the inset graphs, where R represents RMSE.
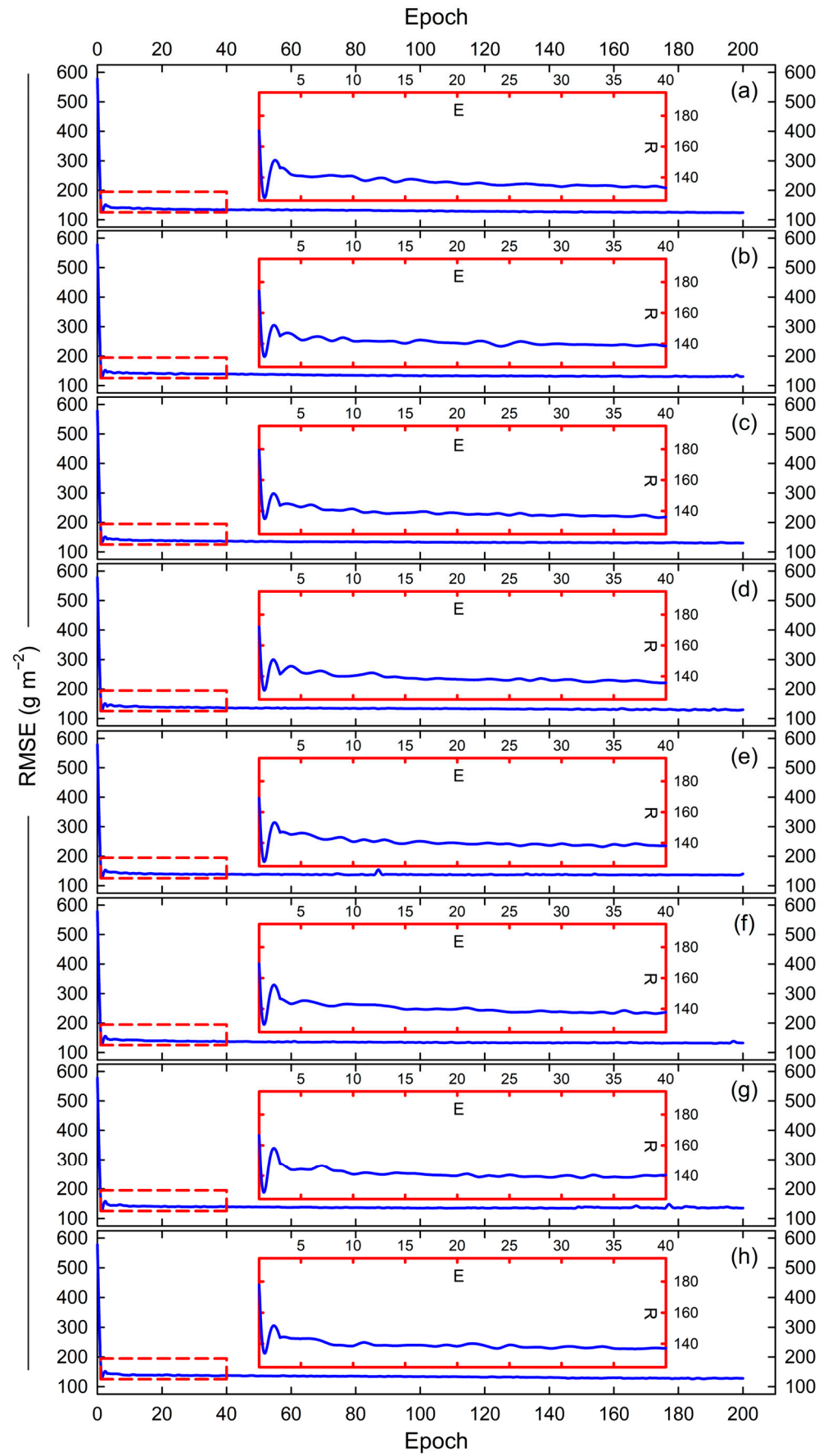
Figure 7. Neural network training progresses to predict cover crop biomass with sigmoid (**a**), tanh (**b**), ReLU (**c**), exponential (**d**), linear (**e**), SELU (**f**), ELU (**g**), and SiLU (**h**) activation functions. Detailed results within the first 40 epochs (E) are shown in the inset graphs, where R represents RMSE.

The ultimate judgement of the neural network model performance in predicting cover crop biomass in this study was based on the 25% of the data set aside for model testing, with the results shown in Table 3 and Figures 8 and 9. The top four configurations providing the best RMSEs are shown in bold in Table 3. The TensorFlow model configured with Adam and the sigmoid activation function at Dense 2 showed the best performance for cover crop biomass prediction, with an RMSE of 96 g m^{-2} (Table 3). This configuration also showed higher values of the Pearson correlation (0.793) and R^2 (0.629) as compared with the other configurations, except for the configuration with Adam and the SiLU activation function, which had a slightly higher Pearson correlation and R^2, at 0.797 and 0.635, respectively, when exploring the connection between predicted and actual values in the test set. The scatter plots of observed values against predicted ones are shown in Figures 8 and 9, providing useful insights regarding the robustness of the different models evaluated in this study. The configuration using the Adam optimizer with the exponential activation function and that using SGD with the sigmoid activation function showed moderate RMSEs of 111 and 118, respectively, but the scatter plots for these configurations showed a clustering phenomenon, indicating that a random data selection for the evaluation might have lowered the variation for these configurations, preventing a more effective test of their robustness (Figures 8d and 9d). On the other hand, the configuration with Adam and Nadam optimizers with a sigmoid activation function (Figure 8a,b) and an Adam optimizer with SELU and SiLU activation functions (Figure 9f,h) visually showed robust performance levels across a good stretch of the observed cover crop DM values. The inset graphs in Figures 8 and 9 provide clear visualizations of the common drawbacks in the prediction of cover crop DM even in this study, even with the best configuration (Adam with sigmoid activation function), that is, the tendency to underpredict at higher biomasses. Some configurations, namely Adadelta and Adgrad optimizers with the sigmoid activation function and Adam with ReLU and exponential activation functions, exhibited the worst performance levels when they made underpredictions at higher observed biomasses (Figure 8f,g and Figure 9c,d).

Table 3. Performance of the TensorFlow models with different optimizers and activation functions and in predicting cover crop biomass.

Optimizer	Activation Function	RMSE (g m^{-2})	Pearson	R^2	Observed		Predicted	
					Min.	Max.	Min.	Max.
Adam	**Sigmoid**	**96**	**0.793**	**0.629**	**290**	**1217**	**335**	**1040**
Nadam	Sigmoid	106	0.677	0.458	367	1110	302	1011
Ftrl	Sigmoid	132	0.512	0.262	293	1223	394	777
SGD	Sigmoid	118	0.481	0.231	327	935	412	792
RMSprop	**Sigmoid**	**103**	**0.694**	**0.482**	**376**	**944**	**324**	**859**
Adadelta	Sigmoid	132	0.638	0.407	281	1326	352	748
Adagrad	Sigmoid	121	0.687	0.471	263	1008	331	779
Adamax	Sigmoid	124	0.656	0.430	316	1057	402	861
Adam	Tanh	108	0.732	0.536	314	1028	342	939
Adam	ReLU	137	0.491	0.240	313	1134	327	813
Adam	Exponential	111	0.654	0.428	342	1264	433	1002
Adam	Linear	148	0.708	0.500	330	1394	354	939
Adam	**SELU**	**99**	**0.676**	**0.458**	**263**	**907**	**369**	**856**
Adam	ELU	133	0.758	0.575	276	1081	265	810
Adam	**SiLU**	**104**	**0.797**	**0.635**	**274**	**974**	**340**	**854**

The rows in bolds indicate the top four best biomass prediction results achieved by the combination of the optimizer and activation functions used in the TensorFlow model in this study.
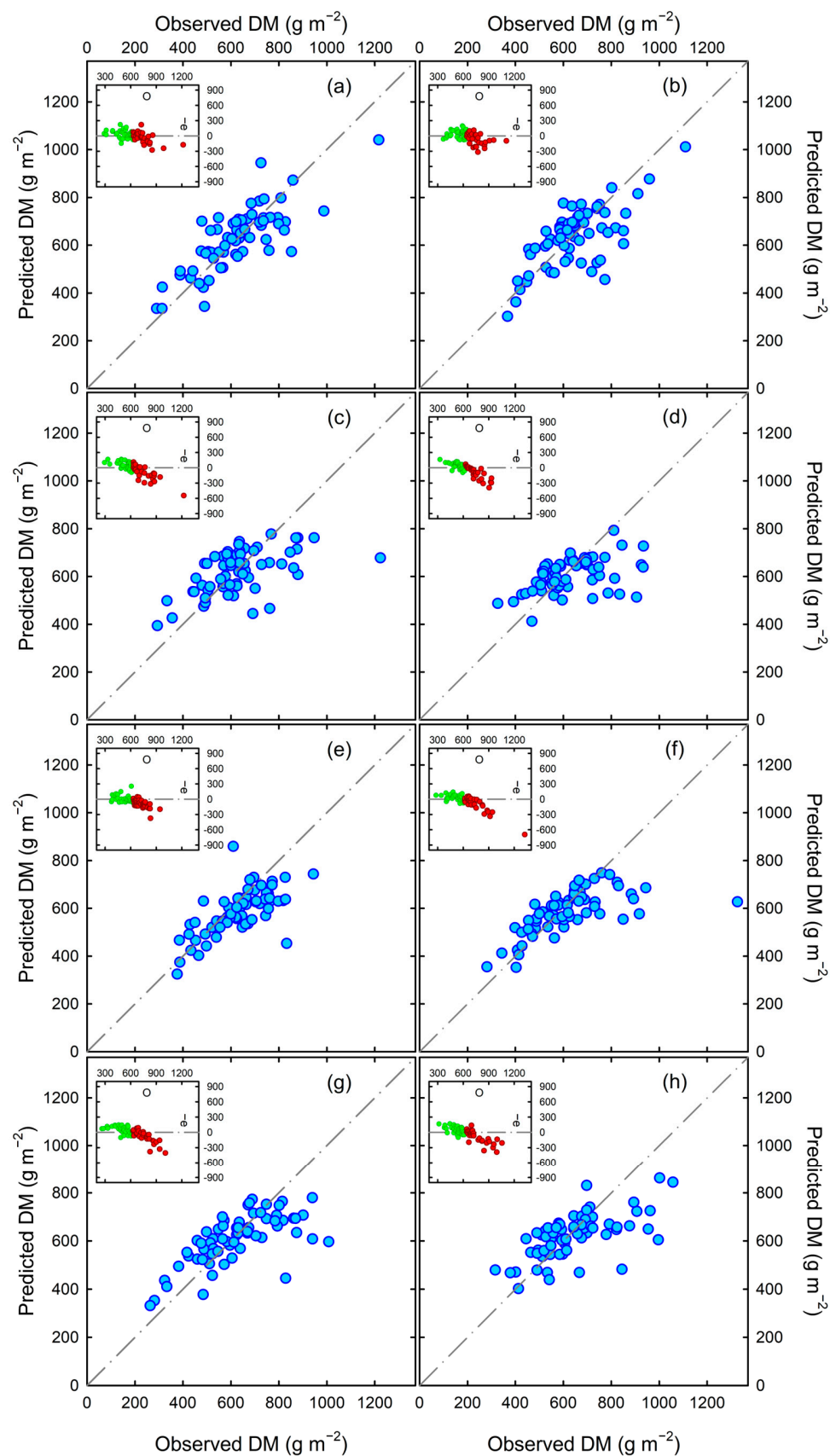
Figure 8. Validation results of cover crop dry matter (DM) prediction with TensorFlow models using Adam (**a**), Nadam (**b**), Ftrl (**c**), SGD (**d**), RMSprop (**e**), Adadelta (**f**), Adagrad (**g**), and Adamax (**h**) Keras optimizers. Residuals expressed as predicted − observed (−e) as a function of the observed DM are shown in graph insets.
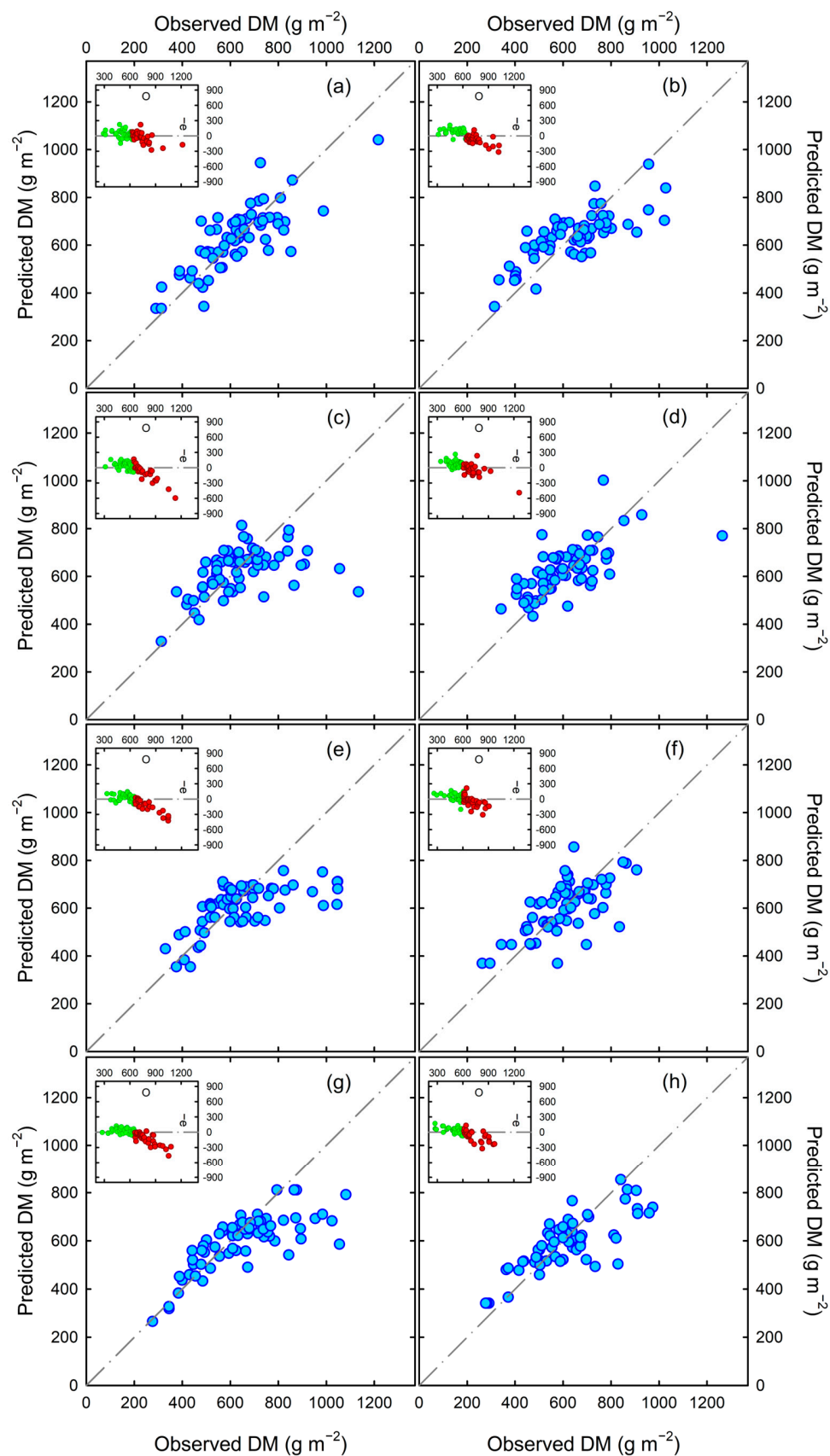
Figure 9. Validation results of cover crop dry matter (DM) prediction with TensorFlow models using sigmoid (**a**), tanh (**b**), ReLU (**c**), exponential (**d**), linear (**e**), SELU (**f**), ELU (**g**), and SiLU (**h**) activation functions. Residuals expressed as predicted − observed (−e) as a function of the observed DM are shown in the inset graphs.

The results of subsequent tests of the best-performing TensorFlow model with the Adam optimizer using all possible combinations of vegetation indices and modeled canopy height (CHM) data are shown in Table 4. The single vegetation index along with the CHM, NDRE, and GNDVI are superior predictors. Nonetheless, substantially lower RMSEs of cover crop biomass predictions were only achieved with combinations of the CHM with at least three VIs, namely, the NDRE, NDVI, PVI (RMSE of 92 g m^{-2}), NDRE, GNDVI, NDVI, PVI (RMSE of 95 g m^{-2}), and all five VIs (RMSE of 96 g m^{-2}).

Table 4. Performance of the TensorFlow model (Adam, sigmoid) with 31 combinations of vegetation indices and modeled canopy height (CHM) in predicting cover crop biomass.

Vegetation Index		GNDVI	NDVI	PVI	VIG
	---------- RMSE (g m^{-2}) ----------				
NDRE	107	-	-	-	-
GNDVI	106	-	-	-	-
NDVI	125	-	-	-	-
PVI	129	-	-	-	-
VIG	121	-	-	-	-
NDRE	-	118	101	113	109
GNDVI	-	-	117	102	144
NDVI	-	-	-	117	132
PVI	-	-	-	-	148
NDRE, GNDVI	-	-	116	112	103
NDRE, NDVI	-	-	-	**92**	122
NDRE, PVI	-	-	-	-	120
GNDVI, NDVI	-	-	-	110	114
GNDVI, PVI	-	-	-	-	139
NDVI, PVI	-	-	-	-	122
NDRE, GNDVI, NDVI	-	-	-	**95**	125
NDRE, GNDVI, PVI	-	-	-	-	133
NDRE, NDVI, PVI	-	-	-	-	134
GNDVI, NDVI, PVI	-	-	-	-	119
NDRE, GNDVI, NDVI, PVI	-	-	-	-	**96**

NDRE, Normalized Difference Red Edge; GNDVI, Green Normalized Difference Vegetation Index; NDVI, Normalized Difference Vegetation Index; PVI, Perpendicular Vegetation Index, VIG, Vegetation Index Green; RMSE, root mean squared error. Results shown in bold are the top 3 best RMSE results obtained by the combination of variables used for biomass prediction in this study.

4. Discussion

The performance of the best deep learning model in this study, with an RMSE of 96 g m^{-2} and nRMSE of 15.3%, is comparable with the results reported from previous studies, as shown in Table 5 [28,52–59]. All previous studies listed in Table 5, except for Hamada et al. [54], deployed UAV remote sensing. The complexity of the methodologies of these previous studies varied from a simple regression approach involving vegetation indices (Vis) [28,52,54] to a complex one involving LiDAR data [56] and biomass modeling [59].

Table 5. Comparison of vegetation DM prediction from this study with other studies.

Authors	Site	Species	Date	Predictor(s)	Method	RMSE	nRMSE	Observed DM		
								Min.	Mean	Max.
								---------------- g m^{-2} ----------------		
This study	Baton Rouge and St. Joseph, LA, USA	Winter cover crops including cereal rye (*Secale cereale* L.) and black oats (*Avena strigosa*)	4 March 2024 24 March 2024	VI (NDRE, GNDVI, NDVI, PVI, VIG) and CHM from UAV	Deep learning with Adam optimizer and sigmoid activation function	96	15.3	290	628	1217
Bendig et al. [28]	Cologne, Germany	Barley (*Hordeum vulgare*)	23 July 2013	VIs and CHM	Multiple linear regression	240	44.6	23	538	1640
Biswal et al. [52]	Kharagpur, West Bengal, India	Lowland rice (*Oryza sativa*)	10 September 2019	VI (15 total) including GNDVI and NDVI from UAV	Multiple linear regression and Random Forest	76	9.1	383	635	842
Sinde-Gonzales et al. [53]	Pichincha, Ecuador	Perennial ryegrass (*Lolium perenne*), annual ryegrass (*Lolium multiflorum*), and kikuyugrass (*Pennisetum clandestinum*)	16 January 2018	DSM, DTM from UAV	f(density factor, predicted volume derived from DTM and DSM)	198	31.0	325	635	1125
Hamada et al. [54]	Brighton, IL, Urbana, IL, Ithaca, NE, and South Shore, SD, USA	Switchgrass for bioenergy	November 2020 December 2020	VI (20 total) including GNDVI and NDVI from Sentinel-2 satellite	f(GNDVI)	60	12.8	119	539	1110
Lussem et al. [55]	Esdorf, Germany	Foxtail grass (*Alopecurus* sp.), timothy grass (*Phleum pratense*), and clover (*Trifolium* sp.)	22 August 2017	VI from visible range (RGB) including ExGI and CHM	f(ExG, CHM)	41.6	17.78	167	234	357
Maesano et al. [56]	Savigliano, Italy	Arundo donax for bioenergy	November 2016	Detailed canopy structure data derived from LiDAR with UAV	f(maximum stem height, stem height with most occurrence, and count of unique stem height)	908	18.17	2133	4542	7867

Table 5. *Cont.*

Authors	Site	Species	Date	Predictor(s)	Method	RMSE	nRMSE	Observed DM		
								Min.	Mean	Max.
								---------------- g m^{-2} ----------------		
Oliveira et al. [57]	Jokioinen, Finland	Silage grass consisting of timothy meadow fescue (*Phleum pratense* and *Festuca pratensis*)	June 2017	Orthomosaic images derived from RGB UAV data	Deep learning using VGG16 with Adadelta optimizer and linear activation function	67	25.2	54	265	546
Theau et al. [58]	Lennoxville, Quebec, Canada	Red clover (*Trifolium pratense*), timothy (*Phleum pratense* L.), birdsfoot trefoil (*Lotus corniculatus*), meadow bromegrass (*Bromus commutatus*), and Kentucky bluegrass (*Poa pratensis* L.)	29 August 2017	VI (total of 9) including NDVI, GNDVI, NDRE, and CHM from UAV	f(DSM, DTM, GNDVI)	132	38	76	348	820
Zhang et al. [59]	Gansu, Inner Mongolia, and Jiangsu, China	Alpine meadow (Poaceae and Cyperaceae), *Stipa glareosa*, *Iris lactea* Pall, *Bassia dasyphylla*, *Spartina alterniflora*, *Suaeda glauca*, and *Phragmites australis*	August 2017	VI and CH from UAV	Biomass model based on CH combined with ExG from RGB	96	15.3	20	628	824

VI, Vegetation Index; CH, Canopy Height; DSM, Digital Surface Model; DTM, Digital Terrain Model; ExG, Excess Greenness; f(x, z, . . .) indicates a function of x, z, and any other variables listed.

It is interesting to note that five out of eight of these previous studies included the canopy height derived from an UAV as key predictor of biomass [53,55,56,58,59]. Only one of these studies deployed deep learning, but their approach involved the use of orthomosaic images as inputs [57] and thus the utilization of machine learning included image analyses. The comparative analysis provided in this report is complete with RMSE and nRMSE, along with the reported statistical data of the observed biomass. In contrast, Poley and McDermid [60] reviewed 46 studies of UAV-based biomass prediction only using the R^2 as the selected metric. Nonetheless, their comprehensive review suggests that the NDVI, GNDVI, and CHM are the most common predictors used in biomass prediction studies. In the present study, the only combinations of vegetation indices (VIs) resulting in a high accuracy of biomass predictions were those that use near-infrared (NIR) spectral data. This finding agrees with Viljanen et al. [61], who through a Random Forest machine learning approach, obtained an improvement in biomass prediction when RGB inputs were complemented with NIR reflectance data.

It is unlikely that improving the sophistication of instruments can further improve the accuracy of biomass prediction, as is evident by the relatively similar results achieved with a methodology deploying LiDAR sensor [56] as compared to the present study without such an expensive instrument. The use of hyperspectral instruments, as tested by Bendig et al. [28], did not significantly improve the prediction of vegetation biomass as compared to a multispectral sensor; in particular, the canopy height approach was found to be ideal, given its satisfactory results and yet practical and economical steps.

Without machine learning, particularly deep learning, previous studies performed to predict the vegetation biomass required multiple steps to derive models using training datasets, with the resulting models being site-specific. In contrast, machine learning provides the sophistication of next-generation data interpretation beyond the conventional multi-step regression approach. Oliveira et al. [57], who also implementing deep learning, found similar findings as the present study, discovering a varied performance in terms of biomass prediction accuracy depending on the combination of model optimizers and architecture. In their case, the Adadelta optimizer with the VGG16 convolutional neural network (CNN) architecture performed the best, with an RMSE of 67 g m^{-2} and R^2 of 0.79, whereas the Adam optimizer with the Inception V3 CNN architecture performed the worst, with an RMSE of 883 g m^{-2} and R^2 of -72.43. The range of results obtained by Oliveira et al. [57] through the different combinations of CNN architectures and optimizers was more extreme than in the present study. The negative R^2 they obtained was indicative that the given CNN architecture and optimizer did not provide an opportunity for the deep learning model to give a positive performance during training, a phenomenon that was lacking in the present study.

While we may point out their similar deep learning setups, such as 200 for the number of epochs, a learning rate of 0.01, and a similar split for testing at 20–25%, it is not feasible to draw a straightforward comparison between the present study and that of Oliveira et al. [57] due to the different natures of their deep learning applications. The deep learning technique used by Oliveira et al. [57] was tailored to make use of UAV natural color (RGB) images for the prediction of vegetation biomass, whereas in the present study, the orthomosaic input data were converted to numerical data of vegetation indices, and we modeled canopy height information prior to their usage to predict vegetation biomass. Moreover, Oliveira et al. [57] focused on the CNN architecture, commonly applied for dealing with image classification tasks, whereas the Keras optimizers and activation functions used in the present study are more suitable for dealing with numerical features and for output prediction.

The drawback of the machine learning approach is the sensitivity of the outcome to the quantity of data used [62]. To achieve sufficient data points for machine learning, there is

an opportunity to leverage a non-destructive and rapid methodology to generate biomass data using rising plate or disk meters (RPMs). Available commercial RPM instruments utilizing ultrasonic technology include the GrassHopper (TrueNorth Technologies, Shannon, Ireland), GrassOmeter (Monford AG Systems Ltd., Dublin, Ireland), Pasture Meter (C-Dax Agricultural Solutions, Palmerston North, New Zealand), and Pasture Reader (Naroaka Enterprises, Narracan, Australia) [55]. The present study highlights the need to address the saturation problem with vegetation indices at high biomass conditions, resulting in the trend of the model underpredicting the biomass in conditions conducive to heavy growth. Comparable results were reported by others who found a saturation of machine learning performance when feature information was sufficiently utilized [63,64]. A new creative approach to using the data may be needed, such as exploring the rate of change in the VI and CHM. In high biomass conditions, differences in absolute values are difficult to detect, and the rates should offer stronger indicators. An example of this is the presence of abiotic or biotic stress causing slight a reduction in VIs and/or the CHM, which can be detected much more efficiently by examining the rates of changes than static variables. This creative approach will be explored in future studies, which will also test the prediction model in more locations and growing seasons.

5. Conclusions

The present study reinforces the finding of previous studies that canopy height estimation along with vegetation indices can be used effectively to predict vegetation biomass. In the present study, the deep learning neural network model with the Adam optimizer and sigmoid activation function performed the best, providing cover crop biomass prediction with a 96 g m^{-2} RMSE and 15.1% nRMSE. These findings underscore the value of combining UAV remote sensing and machine learning for a comprehensive analysis of cover crop traits. By incorporating realistic biophysical mechanisms, this approach effectively captured both the horizontal (vegetation indices) and vertical (canopy height) dimensions of plant growth.

References

1. Dabney, S.M.; Delgado, J.A.; Reeves, D.W. Using winter cover crops to improve soil and water quality. *Commun. Soil Sci. Plant Anal.* **2001**, *32*, 1221–1250. [CrossRef]
2. Ruffatti, M.D.; Roth, R.T.; Lacey, C.G.; Armstrong, S.D. Impacts of nitrogen application timing and cover crop inclusion on subsurface drainage water quality. *Agric. Water Manag.* **2019**, *211*, 81–88. [CrossRef]
3. Steenwerth, K.; Belina, K.M. Cover crops enhance soil organic matter, carbon dynamics and microbiological function in a vineyard agroecosystem. *Appl. Soil Ecol.* **2008**, *40*, 359–369. [CrossRef]

4.   Sanchez, I.; Fultz, L.M.; Lofton, J.; Haggard, B. Cover crops impact on Louisiana corn production and soil properties. *Agrosyst. Geosci. Environ.* **2019**, *2*, 1–8. [CrossRef]

5.   Snapp, S.S.; Swinton, S.M.; Labarta, R.; Mutch, D.; Black, J.R.; Leep, R.; Nyiraneza, J.; O'neil, K. Evaluating cover crops for benefits, costs and performance within cropping system niches. *Agron. J.* **2005**, *97*, 322–332. [CrossRef]

6.   Schappert, A.; Messelhäuser, M.H.; Saile, M.; Peteinatos, G.G.; Gerhards, R. Weed suppressive ability of cover crop mixtures compared to repeated stubble tillage and glyphosate treatments. *Agriculture* **2018**, *8*, 144. [CrossRef]

7.   Bryan, C.J.; Sipes, S.D.; Arduser, M.; Kassim, L.; Gibson, D.J.; Scott, D.A.; Gage, K.L. Efficacy of cover crops for pollinator habitat provision and weed suppression. *Environ. Entomol.* **2021**, *50*, 208–221. [CrossRef]

8.   Mallinger, R.E.; Franco, J.G.; Prischmann-Voldseth, D.A.; Prasifka, J.R. Annual cover crops for managed and wild bees: Optimal plant mixtures depend on pollinator enhancement goals. *Agric. Ecosyst. Environ.* **2019**, *273*, 107–116. [CrossRef]

9.   Herbstritt, S.; Richard, T.L.; Lence, S.H.; Wu, H.; O'Brien, P.L.; Emmett, B.D.; Kaspar, T.C.; Karlen, D.L.; Kohler, K.; Malone, R.W. Rye as an energy cover crop: Management, forage quality, and revenue opportunities for feed and bioenergy. *Agriculture* **2022**, *12*, 1691. [CrossRef]

10.   Kharel, T.P.; Bhandari, A.B.; Mubvumba, P.; Tyler, H.L.; Fletcher, R.S.; Reddy, K.N. Mixed-species cover crop biomass estimation using planet imagery. *Sensors* **2023**, *23*, 1541. [CrossRef]

11.   Swoish, M.; Leme Filho, J.F.D.C.; Reiter, M.S.; Campbell, J.B.; Thomason, W.E. Comparing satellites and vegetation indices for cover crop biomass estimation. *Comp. Electron. Agric.* **2022**, *196*, 106900. [CrossRef]

12.   Dean, J.E.; Weil, R.R. Brassica cover crops for nitrogen retention in the Mid-Atlantic Coastal Plain. *J. Environ. Qual.* **2009**, *38*, 520–528. [CrossRef] [PubMed]

13.   Finney, D.M.; White, C.M.; Kaye, J.P. Biomass production and carbon/nitrogen ratio influence ecosystem services from cover crop mixtures. *Agron. J.* **2016**, *108*, 39–52. [CrossRef]

14.   Wang, S.; Guan, K.; Zhang, C.; Jiang, C.; Zhou, Q.; Li, K.; Qin, Z.; Ainsworth, E.A.; He, J.; Wu, J.; et al. Airborne hyperspectral imaging of cover crops through radiative transfer process-guided machine learning. *Remote Sens. Environ.* **2023**, *285*, 113386. [CrossRef]

15.   Vigneault, P.; LafondLapalme, J.; Deshales, A.; Khun, K.; Sablonniere, S.D.; Fillon, M.; Longchamps, L.; Mimee, B. An integrated data-driven approach to monitor and estimate plant-scale growth using UAV. *ISPRS Open J. Photogramm. Remote Sens.* **2023**, *11*, 100052. [CrossRef]

16.   Jackson, R.D.; Huerte, A.R. Interpreting vegetation indices. *Prev. Vet. Med.* **1991**, *11*, 185–200. [CrossRef]

17.   Rouse, J.; Haas, R.H.; Schell, J.A.; Deering, D. Monitoring Vegetation Systems in the Great Plains with ERTS. In *Third Earth Resources Technology Satellite-1 Symposium—Volume I: Technical Presentations. NASA SP-351*; Freden, S.C., Mercanti, E.P., Becker, M.A., Eds.; NASA: Washington, DC, USA, 1973; pp. 307–317.

18.   Qi, J.; Chehbouini, A.; Huete, A.; Kerr, Y.; Sorooshian, S. A modified soil adjusted vegetation index. *Remote Sens. Environ.* **1994**, *48*, 119–126. [CrossRef]

19.   Prabhakara, K.; Hively, W.D.; McCarty, G.W. Evaluating the relationship between biomass, percent groundcover and remote sensing indices across six winter cover crop fields in Maryland, United States. *Int. J. Appl. Earth Obs. Geoinf.* **2015**, *39*, 88–102. [CrossRef]

20.   Mutanga, O.; Skidmore, A.K. Narrow band vegetation indices overcome the saturation problem in biomass estimation. *Int. J. Remote Sens.* **2004**, *25*, 3999–4014. [CrossRef]

21.   Chen, J.; Gu, S.; Shen, M.; Tang, Y.; Matshushita, B. Estimating aboveground biomass of grassland having a high canopy cover: An exploratory analysis of in situ hyperspectral data. *Int. J. Remote Sens.* **2009**, *30*, 6497–6517. [CrossRef]

22.   Muñoz, J.D.; Finley, A.O.; Gehl, R.; Kravchenko, S. Nonlinear hierarchical models for predicting cover crop biomass using Normalized Difference Vegetation Index. *Remote Sens. Environ.* **2010**, *114*, 2833–2840. [CrossRef]

23.   Payero, J.O.; Neale, C.M.U.; Wright, J.L. Comparison of eleven vegetation indices for estimating plant height of alfalfa and grass. *Appl. Eng. Agric.* **2004**, *20*, 385–393. [CrossRef]

24.   Xie, T.; Li, J.; Yang, C.; Jiang, Z.; Chen, Y.; Guo, L.; Zhang, J. Crop height estimation based on UAV images: Methods, errors, and strategies. *Comput. Electron. Agric.* **2021**, *185*, 106155. [CrossRef]

25.   Hassan, M.A.; Yang, M.; Fu, L.; Rasheed, A.; Zheng, B.; Xia, X.; Xiao, Y.; He, Z. Accuracy assessment of plant height using an unmanned aerial vehicle for quantitative genomic analysis in bread wheat. *Plant Methods* **2019**, *15*, 37. [CrossRef] [PubMed]

26.   Feng, A.; Zhange, M.; Sudduth, K.A.; Vories, E.D.; Zhou, J. Cotton yield estimation from UAV-based plant height. *Trans. ASABE* **2019**, *62*, 393–404. [CrossRef]

27.   Yuan, W.; Li, J.; Bhatta, M.; Shi, Y.; Baenziger, P.S.; Ge, Y. Wheat height estimation using LiDAR in comparison to ultrasonic sensor and UAS. *Sensors* **2018**, *18*, 3731. [CrossRef] [PubMed]

28.   Bendig, J.; Yu, K.; Aasen, H.; Bolden, A.; Bennertz, S.; Broscheeit, J.; Gnyp, M.L.; Bareth, G. Combining UAV-based plant height from crop surface models, visible, and near infrared vegetation indices for biomass monitoring in barley. *Int. J. Appl. Earth Obs. Geoinf.* **2015**, *39*, 79–87. [CrossRef]

29. Brocks, S.; Bareth, G. Estimating barley biomass with crop surface models from oblique RGB imagery. *Remote Sens.* **2018**, *10*, 268. [CrossRef]

30. Zou, J.; Han, Y.; So, S.S. Overview of artificial neural networks. In *Artificial Neural Networks. Methods in Molecular Biology*; Livingstone, D.J., Ed.; Humana Press: Totowa, NJ, USA, 2009; pp. 14–22.

31. Luo, M.; Wang, Y.; Xie, Y.; Zhou, L.; Qiao, J.; Qiu, S.; Sun, Y. Combination of feature selection and catboost for prediction: The first application to the estimation of aboveground biomass. *Forests* **2021**, *12*, 216. [CrossRef]

32. Barnes, E.; Clarke, T.R.; Richards, S.E.; Colaizzi, P.; Haberland, J.; Kostrzewski, M.; Waller, P.; Choi, C.; Riley, E.; Thompson, T.L. Coincident Detection of Crop Water Stress, Nitrogen Status, and Canopy Density using Ground based Multispectral Data. In Proceedings of the Fifth International Conference on Precision Agriculture, Bloomington, MN, USA, 16–19 July 2000; Volume 1619. No. 6.

33. Gitelson, A.A.; Kaufman, Y.J.; Merzlyak, M.N. Use of a green channel in remote sensing of global vegetation from EOS-MODIS. *Remote Sens. Environ.* **1996**, *58*, 289–298. [CrossRef]

34. Rouse, J.W.; Hass, R.H.; Schell, J.A.; Deering, D.W.; Harlan, J.C. *Monitoring the Vernal Advancement and Retrogradation (Green Wave Effect) of Natural Vegetation*; Final Report, RSC 1978-4; Texas A & M University: College Station, TX, USA, 1974; pp. 1–120.

35. Richardson, A.J.; Wiegand, C.L. Distinguishing vegetation from soil background information. *Photogramm. Eng. Remote Sens.* **1977**, *43*, 1541–1552.

36. PIX4Dmapper. The Leading Photogrammetry Software for Professional Drone Mapping. License Activated on 24 April 2022. Version 4.7.5. Available online: https://www.pix4d.com/product/pix4dmapper-photogrammetry-software/ (accessed on 13 November 2024).

37. Setiyono, T. Precise positioning in nitrogen fertility sensing in maize (*Zea mays* L.). *Sensors* **2024**, *24*, 5322. [CrossRef] [PubMed]

38. Geospatial Data Abstraction Library (GDAL)/OGR Simple Features Library (OGR) Contributors. GDAL/OGR Geospatial Data Abstraction Software Library. Open-Source Geospatial Foundation. Available online: https://zenodo.org/records/12545688 (accessed on 11 November 2024).

39. Quantum Geographic Information System (QGIS) Development Team. QGIS Geographic Information System. Version 3.28.1. Open-Source Geospatial Foundation. Available online: http://qgis.org (accessed on 7 December 2024).

40. Voitik, A.; Kravchenko, V.; Pushka, O.; Kutkovetska, T.; Schur, T.; Kocira, S. Comparison of NDVI, NDRE, MSAVI, and NDSI indices for early diagnosis of crop problems. *Agric. Eng.* **2023**, *27*, 47–57. [CrossRef]

41. Hastie, T.; Tibshirani, R.; Friedman, J. *The Elements of Statistical Learning: Data Mining, Inference, and Prediction*, 2nd ed.; Springer Science Business Media LLC.: New York, NY, USA, 2009.

42. Abadi, M.; Barham, P.; Chen, J.; Chen, Z.; Davis, A.; Dean, J.; Devin, M.; Ghemawat, S.; Irving, G.; Isard, M.; et al. TensorFlow: A system for large-scale machine learning. In Proceedings of the 12th USENIX Symposium on Operating Systems Design and Implementation (OSDI'16), Savannah, GA, USA, 2–4 November 2016.

43. Kingma, D.P.; Ba, J. Adam: A Method for Stochastic Optimization. *arXiv* **2014**, arXiv:1412.6980. [CrossRef]

44. Dozat, T. Incorporating Nesterov Momentum into Adam. Workshop Track. In Proceedings of the International Conference on Learning Representation, San Juan, Puerto Rico, 2–4 May 2016.

45. McMahan, H.B.; Holt, G.; Sculley, D.; Young, M.; Ebner, D.; Grady, J.; Nie, L.; Phillips, T.; Davydov, E.; Golovin, D.; et al. Ad Click Prediction: A View from the Trenches. In Proceedings of the 19th ACM SIGKDD International Conference on Knowledge Discovery and Data Mining, Chicago, IL, USA, 11–14 August 2013; pp. 1222–1230.

46. Chollet, F.; Watson, M.; Bursztein, E.; Zhu, Q.S.; Jin, H. Keras. GitHub. 2015. Available online: https://github.com/keras-team/keras (accessed on 14 December 2024).

47. Aggarwal, C.C. *Neural Networks and Deep Learning*; Springer: Cham, Switzerland, 2018; Volume 10, No. 978.

48. Zeiler, M.D. ADADELTA: An adaptive learning rate method. *arXiv* **2017**, arXiv:1212.5701. [CrossRef]

49. Duchi, J.; Hazan, E.; Singer, Y. Adaptive sub-gradient methods for online learning and stochastic optimization. *J. Mach. Learn. Res.* **2011**, *12*, 2121–2159.

50. Klambauer, G.; Unterthiner, T.; Mayr, A.; Hochreiter, S. Self-normalizing neural networks. *arXiv* **2017**, arXiv:1706.02515. [CrossRef]

51. Ramachandran, P.; Zoph, B.; Le, Q.V. Searching for activation functions. *arXiv* **2017**, arXiv:1710.05941. [CrossRef]

52. Biswal, S.; Pathak, N.; Catterjee, C.; Mailapalli, D.R. Estimation of aboveground biomass from spectral and textural characteristics of paddy crop using UAV-multispectral images and machine learning techniques. *Geocarto Int.* **2024**, *39*, 2364725. [CrossRef]

53. Sinde-Gonzales, I.; Gil-Decampo, M.; Arza-Garcia, M.; Grefa-Sanches, J.; Yanez-Simba, D.; Perez-Guerrero, P.; Abril-Porras, V. Biomass estimation of pasture plots with multitemporal UAV-based photogrammetric surveys. *Int. J. Appl. Earth Obs. Geoinf.* **2021**, *101*, 102355. [CrossRef]

54. Hamada, Y.; Zumpf, C.R.; Caccho, J.F.; Lee, D.K.; Lin, C.-H.; Boe, A.; Heaton, E.; Mitchell, R.; Negri, M.C. Remote sensing-based estimation of advanced perennial grass biomass yields for bioenergy. *Land* **2021**, *10*, 1221. [CrossRef]

55. Lussem, U.; Bolten, A.; Menne, J.; Gnyp, M.L.; Schellberg, J.; Bareth, G. Estimating biomass in temperate grassland with high resolution canopy surface models from UAV-based RGB images and vegetation indices. *J. Appl. Remote Sens.* **2019**, *3*, 034525. [CrossRef]

56. Maesano, M.; Khoury, S.; Nakhle, F.; Firrincieli, A.; Gay, A.; Tauro, F.; Harfouche, A. UAV-based LiDAR for high-throughput determination of plant height and above-ground biomass of the bioenergy grass *Arundo donax*. *Remote Sens.* **2020**, *12*, 3464. [CrossRef]

57. Oliveira, R.A.; Marcato Junor, J.; Costa, C.S.; Nasi, R.; Koivumaki, N.; Niemelainen, O.; Kaivosoja, J.; Nyholm, L.; Pistori, H.; Honkavaara, E. Silage grass sward nitrogen concentration and dry matter yield estimation using deep regression and RGB images captured by UAV. *Agronomy* **2022**, *6*, 1352. [CrossRef]

58. Theau, J.; Lauzier-Hudon, E.; Aube, L.; Devillers, N. Estimation of forage biomass and vegetation cover in grasslands using UAV imagery. *PLoS ONE* **2021**, *16*, e0245784. [CrossRef] [PubMed]

59. Zhang, H.; Sun, Y.; Chang, L.; Qin, Y.; Chen, J.; Qin, Y.; Du, J.; Yi, S.; Wang, Y. Estimation of grassland canopy height and aboveground biomass at the quadrat scale using unmanned aerial vehicle. *Remote Sens.* **2018**, *10*, 851. [CrossRef]

60. Poley, L.; McDermid, G.J. A systematic review of the factors influencing the estimation of vegetation aboveground biomass using unmanned aerial systems. *Remote Sens.* **2020**, *12*, 1052. [CrossRef]

61. Viljanen, N.; Honkavaara, E.; Näsi, R.; Hakala, T.; Niemeäinen, O.; Kaivosoja, J. A novel machine leaning method for estimating biomass of grass swards using a photogrammetric canopy height model, images, and vegetation indices captured by a drone. *Agriculture* **2018**, *8*, 70. [CrossRef]

62. Setiyono, T.; Gentimis, T.; Rontani, F.; Duron, D.; Bortolon, G.; Adhikari, R.; Acharya, B.; Han, K.J.; Pitman, W.D. Application of TensorFlow model for identification of herbaceous mimosa (*Mimosa strigillosa*) from digital images. *Smart Agric. Technol.* **2024**, *7*, 100400. [CrossRef]

63. Yu, D.; Zha, T.; Sun, Z.; Li, J.; Jin, X.; Zhu, W.; Bian, J.; Zheng, Y.; Su, Z. Deep convolutional neural networks for estimating maize above-ground biomass using multi-source UAV images: A comparison with traditional machine learning algorithms. *Prec. Agric.* **2023**, *24*, 92–113. [CrossRef]

64. Vahidi, M.; Shafian, S.; Thomas, S.; Maguire, R. Pasture biomass estimation using ultra-high resolution RGB UAVs images and deep learning. *Remote Sens.* **2023**, *15*, 5714. [CrossRef]